Thermal effusivity measurements of thermal insulators using the photopyroelectric technique in the front configuration

Agustín Salazar[1,*], Alberto Oleaga[1], Arantza Mendioroz[1], and Estibaliz Apiñaniz[2]

[1] Departamento de Física Aplicada I, Escuela de Ingeniería de Bilbao, Universidad del País Vasco UPV/EHU, Plaza Ingeniero Torres Quevedo 1, 48013 Bilbao, Spain.
[2] Departamento de Física Aplicada I, Escuela Universitaria de Ingeniería de Vitoria-Gasteiz, Universidad del País Vasco UPV/EHU, Nieves Cano 12, 01006 Vitoria-Gasteiz, Spain.
* Corresponding author.
E-mail Address: agustin.salazar@ehu.es

Abstract

In the photopyroelectric (PPE) technique in the front configuration one surface of a pyroelectric sensor is illuminated by a modulated laser beam, whereas the other surface is in contact with the sample under study. A frequency scan of the PPE signal allows to measure the thermal effusivity of liquids. Recently, it has been applied to solid samples, by taking into account the effect of the thin grease layer used to guarantee the thermal contact between sample and sensor. In this work, we extend this method to address the challenge of measuring the effusivity of thermal insulators accurately. We have developed a complete model of the PPE signal generation, including heat losses by convection, radiation and conduction to the surrounding gas. Besides, very thin pyroelectric sensors are used since they enhance the sensitivity of the PPE signal to the sample effusivity. Moreover, the sample is placed directly in contact with the sensor, without using any coupling grease, to avoid polluting porous samples. PPE measurements on several thermal insulators (paper, cork, wood and foam) indicate that this method is well suited to retrieve the thermal effusivity of insulators precisely.

Keywords: thermal effusivity, photopyroelectric technique, photothermal techniques, thermal insulators

1. Introduction

In the photopyroelectric (PPE) technique in the front configuration the sample under study is in thermal contact with a pyroelectric plate, whereas the other surface of the pyroelectric sensor is illuminated by a modulated laser beam. This technique was proposed by Dadarlat and coworkers in 1990 [1] and, since then, it has been used to measure the thermal effusivity (*e*) of liquids successfully [2,3]. In fact, a frequency scan of the PPE signal is highly sensitive to the thermal effusivity of the liquid in contact with the pyroelectric sensor [4,5]. However, for solid samples a grease layer must be applied to guarantee the thermal contact between sample and sensor. This grease layer modifies the PPE signal in such a way that the thermal effusivity of solid samples cannot be retrieved precisely. In this way, Zammit and coworkers proposed to use the phase of the self-normalized PPE signal, using a transparent pyroelectric sensor with transparent electrodes (Indium Tin Oxide) and transparent coupling grease [6]. They demonstrated that, working in the thermally thin regime (low frequencies), the PPE signal does not depend on the grease layer and that the diffusivity and effusivity of the solid sample can be obtained simultaneously. However, the frequency scans from which the thermal effusivity is obtained are a bit wavy (see Figs. 5, 6 and 8 in Ref. 6).

To overcome these drawbacks, authors proposed in a recent paper to perform a frequency scan of the PPE signal in the front configuration, but taking into account the thickness of the coupling grease placed between sample and sensor [7]. The PPE signal was shown to depend solely on the solid effusivity and the thickness of the grease layer, due to the fact that the thickness of the pyroelectric sensor and its thermal properties are known, as it happens with the thermal properties of the grease. Therefore, in order to obtain the thermal effusivity of the solid, it was enough to fit the experimental frequency scan of the PPE signal to the theoretical model, where the effect of the fluid layer is accounted for. The method was checked measuring the already known thermal effusivity of a wide range of solids, from bad to high thermal conductors (from polymers and glasses to metals).

The aim of this work is to measure the effusivity of thermal insulators. Polymers are the homogeneous materials with the lowest thermal effusivity (500-700 $Ws^{0.5}m^{-2}K^{-1}$). On the other hand, air has a thermal effusivity of 5.5 $Ws^{0.5}m^{-2}K^{-1}$. Good thermal insulators are highly porous materials: the higher the porosity the lower the thermal effusivity, approaching the air value. This is the case, for instance, of wood, paper, cork and foam. The method developed in Ref. 7 fails when dealing with thermal insulators. To extend it, the following improvements have been introduced. (a) Heat losses by convection, radiation and conduction to the surrounding gas, which are negligible when measuring good thermal conductors, are included in the model. (b) A very thin pyroelectric sensor is used to enhance the sensitivity of the PPE signal corresponding to samples of extremely low sample effusivity. (c) To avoid contaminating porous samples, these are placed directly in contact with the sensor without using any coupling grease. PPE measurements performed on a set of thermal insulators covering the effusivity range 25 - 500 $Ws^{0.5}m^{-2}K^{-1}$ confirm the ability of the method to obtain the thermal effusivity of insulators accurately.

It is worth mentioning that there are other photothermal techniques (optical excitation and thermal detection) that allow measuring the thermal transport properties of solid samples [8]. Among them, photothermal radiometry (PTR), where the sample is excited by a light beam and its thermal emission is recorded by an infrared detector, is the most acknowledge one to measure the thermal effusivity of solids [9,10]. This is a non-contact technique that allows measuring large surfaces. The PPE technique, instead, is a contact technique and the size of the samples to be studied is restricted by the pyroelectric sensor area, about 1 cm^2. Its main advantage is the outstanding signal to noise ratio and the possibility to measure the temperature dependence of the thermal properties from a single temperature scan [6,7].

2. Theory

Fig. 1a shows the geometry of the problem we are dealing with. It consists of a four-layer system made of an infinitely thick air layer, an opaque pyroelectric slab of thickness L_p, a fluid layer of thickness L_f and an infinitely thick solid sample. A modulated light beam (intensity I_o and frequency f) heats the whole surface of the pyroelectric sensor in contact with the air. In this way, heat propagates just along the z-axis. The PPE signal (S) is proportional to the spatially averaged temperature change of the pyroelectric sensor induced by the optical heating $\langle T_p \rangle$ [11],

$$S = ab\langle T_p \rangle = ab\frac{1}{L_p}\int_{-L_p}^{0} T_p(z)dz, \tag{1}$$

where a is a frequency-independent factor that depends on the physical properties of the detector (pyroelectric coefficient, dielectric constant and permittivity) and b is a frequency-dependent factor that accounts for the influence of the detection electronics.

By solving the heat diffusion equation, the temperature change of each layer due to the optical heating is given by

$$T_g(z) = Ge^{-q_g z} \tag{2a}$$

$$T_p(z) = Ae^{q_p z} + Be^{-q_p z} \tag{2b}$$

$$T_f(z) = Ce^{q_f (z+L_p)} + Ee^{-q_f (z+L_p)} \tag{2c}$$

$$T_s(z) = Fe^{q_s (z+L_p+L_f)}, \tag{2d}$$

where $q = \sqrt{i\omega / D}$, D is the thermal diffusivity and $\omega = 2\pi f$. Subscripts p, f and s stand for pyroelectric detector, coupling fluid and sample respectively. From the boundary conditions at the interfaces, the six constants A to G are determined:

(a) Temperature continuity:

$$T_g\big|_{z=0} = T_p\big|_{z=0} \qquad T_p\big|_{z=-L_p} = T_f\big|_{z=-L_p} \qquad T_f\big|_{z=-(L_p+L_f)} = T_s\big|_{z=-(L_p+L_f)} \tag{3a}$$

(b) Heat flux continuity:

$$K_p \frac{dT_p}{dz}\bigg|_{z=-L_p} = K_f \frac{dT_f}{dz}\bigg|_{z=-L_p} \qquad K_f \frac{dT_f}{dz}\bigg|_{z=-(L_p+L_f)} = K_s \frac{dT_s}{dz}\bigg|_{z=-(L_p+L_f)} \tag{3b}$$

(c) Illumination and heat losses at the front surface:

$$K_p \frac{dT_p}{dz}\bigg|_{z=0} = K_g \frac{dT_g}{dz}\bigg|_{z=0} + \frac{I_o \eta}{2} - hT_g\big|_{z=0}. \tag{3c}$$

Here K is the thermal conductivity, η is the fraction of the laser beam energy absorbed by the sample and h is the combined heat transfer coefficient by convection and radiation. As the surface temperature rise is small, the heat rate dissipated from the surfaces can be regarded as a linear function of the temperature. By substituting Eqs. (2) into Eqs. (3), the temperature change of the pyroelectric slab, T_p, is obtained. Then, from Eq. (1), the PPE signal (S) is calculated.

To eliminate the frequency dependence of the detection electronics, factor b in Eq. (1), we divide the PPE signal corresponding to the four-layer system by the PPE signal obtained for the naked pyroelectric plate. Its temperature change can be obtained by solving the heat diffusion equation for the three-layer system shown in Fig. 1b

$$T_{gf}'(z) = G'e^{-q_g z} \tag{4a}$$

$$T_p^{'}(z) = A'e^{q_p z} + B'e^{-q_p z} \tag{4b}$$

$$T_{gr}^{'}(z) = C'e^{q_g (z+L_p)}. \tag{4c}$$

Here subscripts *gf* and *gr* stand for the gas at the front surface and the gas at the rear surface respectively. The four constants *A*' to *G*' are obtained from the boundary conditions at the interfaces:

(a) Temperature continuity:

$$T_{gf}^{'}\Big|_{z=0} = T_p^{'}\Big|_{z=0} \qquad T_p^{'}\Big|_{z=-L_p} = T_{gr}^{'}\Big|_{z=-L_p} \tag{5a}$$

(b) Illumination and heat losses at the surfaces:

$$K_p \frac{dT_p^{'}}{dz}\bigg|_{z=0} = K_g \frac{dT_{gf}^{'}}{dz}\bigg|_{z=0} + \frac{I_o}{2} - hT_{gf}^{'}\Big|_{z=0} \qquad K_p \frac{dT_p^{'}}{dz}\bigg|_{z=-L_p} = K_g \frac{dT_{gr}^{'}}{dz}\bigg|_{z=-L_p} + hT_{gr}^{'}\Big|_{z=-L_p}, \tag{5b}$$

where we have assumed that coefficient *h* is the same at both surfaces.

Finally, the normalized PPE signal (S_n) writes

$$S_n = \frac{S_{four-layer}}{S_{pyro}} = \frac{ab\langle T_p \rangle_{four-layer}}{ab\langle T_p \rangle_{pyro}} = \frac{2A0(A1+A2)}{B1\cosh(q_f L_f) + B2\sinh(q_f L_f)}, \tag{6}$$

where

$$A0 = \left(\frac{e_g}{e_f} + \frac{h}{e_f\sqrt{i\omega}}\right)\cosh\left(\frac{q_p L_p}{2}\right) + \frac{e_p}{e_f}\sinh\left(\frac{q_p L_p}{2}\right), \tag{7a}$$

$$A1 = \frac{e_p}{e_f}\cosh\left(\frac{q_p L_p}{2}\right)\left(\cosh(q_f L_f) + \frac{e_s}{e_f}\sinh(q_f L_f)\right), \tag{7b}$$

$$A2 = \sinh\left(\frac{q_p L_p}{2}\right)\left(\frac{e_s}{e_f}\cosh(q_f L_f) + \sinh(q_f L_f)\right), \tag{7c}$$

$$B1 = \frac{e_p}{e_f}\left(\frac{e_g}{e_f} + \frac{e_s}{e_f} + \frac{h}{e_f\sqrt{i\omega}}\right)\cosh(q_p L_p) + \left[\left(\frac{e_p}{e_f}\right)^2 + \frac{e_s}{e_f}\left(\frac{e_g}{e_f} + \frac{h}{e_f\sqrt{i\omega}}\right)\right]\sinh(q_p L_p), \tag{7d}$$

$$B2 = \frac{e_p}{e_f}\left[1 + \frac{e_s}{e_f}\left(\frac{e_g}{e_f} + \frac{h}{e_f\sqrt{i\omega}}\right)\right]\cosh(q_p L_p) + \left[\frac{e_g}{e_f} + \frac{h}{e_f\sqrt{i\omega}} + \left(\frac{e_p}{e_f}\right)^2\frac{e_s}{e_f}\right]\sinh(q_p L_p). \tag{7e}$$

As can be seen, the frequency dependence of the detection electronics (*b*) can be eliminated by considering the normalized signal. Moreover, the normalized signal does not depend on the laser intensity I_o either. Eqs. (6) and (7) have been written to highlight the correlations between six independent parameters: $L_f/\sqrt{D_f}$, $L_p/\sqrt{D_p}$, e_g/e_f, e_s/e_f, e_p/e_f and *h*. In PPE experiments L_p, D_p, e_p, e_g and e_f are known, and thus only three unknowns are retained: the fluid "thermal thickness" $L_f/\sqrt{D_f}$, the heat losses coefficient *h* and the effusivity ratio e_s/e_f. Therefore, a fitting of the frequency scan of the normalized PPE signal, S_n, to Eq. (6) gives the thermal effusivity we seek, e_s, together with two by-products: $L_f/\sqrt{D_f}$ and *h*.

This method is valid regardless of the selected coupling fluid. As this work is addressed to thermal insulators and taking into account that many of them are highly porous materials, we propose to put the sample directly in contact with the pyroelectric sensor, without any coupling grease, to avoid damaging the sample. This means that there is a very

thin air layer of several tens of micrometers between sample and sensor. It is worth mentioning that a radiative heat transfer between sensor and sample should be added to the pure conductive transfer. However, it has been demonstrated that when the air layer thickness is smaller than the thermal diffusion length this radiative transfer is completely negligible [12,13].

3. Numerical simulations

All the numerical simulations shown in this section have been performed for a $LiTaO_3$ pyroelectric sensor (D_p = 1.50×10^{-6} m^2/s and e_p = 3750 Ws$^{0.5}$m^{-2}K^{-1}) and air for both, the coupling fluid and the surrounding medium ($e_f = e_g = e_{air}$ = 5.5 Ws$^{0.5}$m^{-2}K^{-1} and $D_f = D_g = D_{air}$ = 21×10^{-6} m^2/s).

In Fig. 2 we show the numerical simulations of the frequency dependence of the phase and amplitude of the normalized PPE signal, Ψ_n and $|S_n|$, for an intermediate thermal effusor (e_s = 1000 Ws$^{0.5}$m^{-2}K^{-1}) and for a bad thermal effusor (e_s = 100 Ws$^{0.5}$m^{-2}K^{-1}). The lowest frequency is f = 0.4 Hz, which is the lowest frequency we have used in the experiments. Two sensor thicknesses are studied: L_p = 320 μm and L_p = 75 μm. The black lines are the simulations neglecting heat losses (e_g = 0 and h = 0) whereas the red lines are the simulations including typical values of heat losses at ambient temperature (e_g = 5.5 Ws$^{0.5}$m^{-2}K^{-1} and h = 10 Wm^{-2}K^{-1}). In the simulations we have kept fixed the coupling fluid "thermal thickness", $L_f / \sqrt{D_f}$ = 0.01 s$^{0.5}$, which corresponds to a realistic air layer of 45 μm. Several features of Fig. 2 deserve comment. (a) On the one hand, the amplitude and phase contrasts decrease as the thermal effusivity of the sample diminishes; this result was already pointed out in a previous paper [7]. (b) For a given value of the sample effusivity, the amplitude and phase contrasts are shifted to higher frequencies as the sensor thickness decreases. According to this result and taking into account our experimental lowest frequency (0.4 Hz), using thin pyroelectric sensors when dealing with thermal insulators is highly recommended. (c) The effect of heat losses cannot be neglected when measuring the thermal effusivity of insulators.

In the remaining of the manuscript only the phase of the normalized signal will be calculated since it will be used in the experiments to obtain the thermal effusivity. Actually, unlike the amplitude of the normalized PPE signal, the phase remains unaffected by the intensity instability of the laser.

In Fig. 3 we analyze the influence of the three unknown parameters ($L_f / \sqrt{D_f}$, h and e_s) on the frequency spectrum of Ψ_n. We have selected a thin pyroelectric sensor, L_p = 75 μm, since it produces a higher phase contrast than the thicker one. The effect of $L_f / \sqrt{D_f}$ is analyzed in Fig. 3a. Simulations have been performed with e_s = 100 Ws$^{0.5}$m^{-2}K^{-1} and h = 10 Wm^{-2}K^{-1}. Four values of the "thermal thicknesses" of the coupling fluid have been considered: 0.005, 0.01, 0.02 and 0.05 s$^{0.5}$. As can be seen, the higher the "thermal thickness", the lower the phase contrast. However, the most important feature is that the "thermal thickness" mainly influences the frequency at which Ψ_n starts rising. The effect of h is analyzed in Fig. 3b. Simulations have been performed with e_s = 100 Ws$^{0.5}$m^{-2}K^{-1} and $L_f / \sqrt{D_f}$ = 0.01 s$^{0.5}$. Four values of the heat losses coefficient have been considered: 0, 5, 10 and 20 Wm^{-2}K^{-1}. As can be seen, the higher the heat losses are, the lower the phase contrast is. However, its influence is only significant at low frequencies. Actually, the frequency at which Ψ_n starts rising remains unaffected. Finally, the effect of e_s is analyzed in Fig. 3c. Simulations have been performed with h = 10 Wm^{-2}K^{-1} and $L_f / \sqrt{D_f}$ = 0.01 s$^{0.5}$. Four values of the thermal effusivity of the sample have been considered: 50, 75, 100 and 150 Ws$^{0.5}$m^{-2}K^{-}

[1]. All of them correspond to thermal insulators, which are the target of this work. As it is expected, the lower the effusivity, the lower the phase contrast. Moreover, its influence is significant at intermediate frequencies. Note that the frequency at which Ψ_n starts rising remains unaffected.

It is worth noting that, according to Fig. 3, the sensitivity of Ψ_n to the three unknown parameters ($L_f / \sqrt{D_f}$, h and e_s) takes place at different frequencies. In fact, $L_f / \sqrt{D_f}$ is more sensitive at high frequencies, h at low frequencies and the thermal effusivity at intermediate frequencies. To verify this result, we have calculated the sensitivity of Ψ_n to a given quantity x, which is defined as [14]

$$Sy(x) = x\frac{\partial \Psi_n}{\partial x}, \quad \text{with } x = L_f / \sqrt{D_f}, h \text{ and } e_s. \tag{8}$$

In Fig. 4 we plot the simulations of the frequency scan of $Sy(L_f / \sqrt{D_f})$, $Sy(h)$ and $Sy(e_s)$ for a poor thermal conductor (e_s = 100 $Ws^{0.5}m^{-2}K^{-1}$), with h = 10 $Wm^{-2}K^{-1}$ and $L_f / \sqrt{D_f}$ = 0.01 $s^{0.5}$. Simulations have been performed for a pyroelectric sensor 75 μm thick, which is more sensitive than a thicker one. As can be seen, the three curves are not proportional showing that the three quantities are not correlated. Moreover, as expected from Fig. 3, the highest sensitivity to $L_f / \sqrt{D_f}$ occurs at a higher frequency than the largest sensitivity to e_s, which in its turn occurs at a higher frequency than the largest sensitivity to h.

In Fig. 5a we show the frequency dependence of the sensitivity of Ψ_n to e_s, $Sy(e_s)$, for several effusivity values. Calculations have been performed with L_p = 75 μm, h = 10 $Wm^{-2}K^{-1}$ and $L_f / \sqrt{D_f}$ = 0.01 $s^{0.5}$. As can be seen, the highest sensitivity corresponds to e_s in the range 200-500 $Ws^{0.5}m^{-2}K^{-1}$, but there is a good enough sensitivity in the range 50 - 2000 $Ws^{0.5}m^{-2}K^{-1}$. For extremely poor thermal effusors (e_s < 50 $Ws^{0.5}m^{-2}K^{-1}$), the sensitivity decreases, indicating the difficulty of measuring the thermal effusivity of extremely poor effusors. On the other hand, for good effusors (e_s > 2000 $Ws^{0.5}m^{-2}K^{-1}$) the sensitivity drastically drops, indicating that for these materials the use of a coupling grease between sample and sensor is more appropriate [7]. Finally, in Fig. 5b we show the frequency dependence of the sensitivity of Ψ_n to e_s for several $L_f / \sqrt{D_f}$ values. Calculations have been performed with e_s = 100 $Ws^{0.5}m^{-2}K^{-1}$, L_p = 75 μm and h = 10 $Wm^{-2}K^{-1}$. This result indicates that the largest sensitivity arises when the thermal contact between sample and sensor is perfect, i.e. in the absence of a coupling air layer. As the air coupling layer increases the sensitivity is reduced and shifted to lower frequencies. Anyway, the sensitivity is good enough up to $L_f / \sqrt{D_f}$ = 0.04 $s^{0.5}$, which means an air layer thickness up to 150 μm.

The numerical simulations performed in this section indicate that the phase of the normalized PPE signal, Ψ_n, depends on three fitting parameters ($L_f / \sqrt{D_f}$, h and e_s), which are not correlated. Accordingly, the thermal effusivity of the sample can be retrieved from a multiparametric fitting of the experimental frequency scan of the phase of the normalized PPE signal, Ψ_n. Moreover, the best experimental conditions to measure the thermal effusivity of thermal insulators require the use of a thin sensor plate together with the thinnest possible air layer between sensor and sample.

4. Experimental results

In order to assess the method we have performed PPE measurements on a homogeneous polymer with well established thermal properties: polyether-ether-ketone

(PEEK). A 4 mm thick PEEK plate has been placed directly on top of a $LiTaO_3$ pyroelectric sensor without using any thermal grease. Two sensor thicknesses have been used: 84 and 320 μm. The free surface of the pyroelectric sensor has been heated by a diode laser (λ = 656 nm, 50 mW, beam diameter of 5 mm). A computer driven modulation of the diode current provides a modulated laser output, and a lock-in reference. The PPE current produced by the pyroelectric sensor is measured by a digital lock-in amplifier. Fig. 6 shows the frequency scan of the phase of the normalized PPE for the PEEK sample using both sensors. Measurements have been performed at room temperature. In order to guarantee 1D heat propagation, the lowest frequency we used was 0.4 Hz. Logarithmic spacing of data points on frequency scans has been used since it has been demonstrated to be superior to linear spacing [15]. Dots are the experimental data and the continuous line is the best fitting to Eq. (6). Due to the high sensitivity and low noise of the $LiTaO_3$ sensor together with the noise reduction provided by the lock-in amplifier, the data phase noise remains smaller than 0.05º. The retrieved value of the thermal effusivity of PEEK is the same for both sensors within the experimental uncertainty, and is in good agreement with the literature values (see Table 1). The uncertainty corresponding to the thinner sensor is a bit lower due to its higher sensitivity and therefore, it has been used for the remaining of the experiments. The fitted value of $L_f / \sqrt{D_f}$ is 0.005 $s^{0.5}$, which corresponds to an air thicknesses of 25 μm, and depends mainly on the roughness of the sample surface. Finally, the fitted value of h is 10 $Wm^{-2}K^{-1}$, which is a quite realistic value for radiation and convection at room temperature [16].

After validating the method, we have applied it to characterize the thermal effusivity of several isotropic thermal insulators: watercolour paper, cork and extruded polystyrene (XPS) foams. In the case of XPS foams we worked with two samples from different manufacturers. They differ on the pore size and we named them according to their colour: yellow (pore size 300±100 μm) and green (pore size 500±200 μm). Fig. 7a shows the frequency scan of Ψ_n for these materials (only yellow XPS foam is plotted, since the frequency scan of the green XPS is very similar). Dots are the experimental data and the continuous lines are the best fittings to Eq. (6). The retrieved effusivity values are given in Table 1. In all measurements $L_f / \sqrt{D_f}$ falls within the range 0.005-0.015 $s^{0.5}$, which corresponds to reasonable air thicknesses of 25-75 μm. As explained before, the air thickness depends on the roughness of the sample surface. In the same way, h falls within the range 5-15 $Wm^{-2}K^{-1}$.

We have also studied the thermal effusivity of Basotect® foam, an extremely lightweight foam (the density is only 9 kg/m^3). It is a flexible, open-cell foam made from melamine resin. Its characteristic feature is the three-dimensional network structure consisting of slender and therefore easily flexed filaments. The frequency scan of Ψ_n is shown in Fig. 7a. Note that the maximum phase contrast hardly reaches 1.8º. Accordingly, the retrieved effusivity is extremely low (see Table 1).

In Fig. 7b we show the frequency scans for two anisotropic insulators: beech wood and balsa wood. The first one is a quite hard wood whereas the second one is a soft, low density wood indicating a higher degree of porosity and, therefore, a lower effusivity value is expected. As their thermal transport properties are anisotropic, measurements have been performed in the direction perpendicular to the growth rings ($\perp$) and in the direction parallel ($\parallel$) to them. The retrieved values of the thermal effusivity are given in Table 1.

In homogeneous materials, the physical properties are well established regardless the manufacturer or the particular piece. In the case of heterogeneous materials, instead, the physical properties vary depending on the manufacturer and/or on the specimen under study. This is just the case of the samples studied in this work. For instance, in the case of paper it has been reported that the thermal conductivity varies from 0.081 to 0.182 $Wm^{-1}K^{-1}$

depending on the density (porosity) [17]. Regarding cork, we worked with insulation corkboard, which is an agglomerate of granules of cork. There is a great commercial variety depending on the density and on the pores sizes [18,19]. On the other hand, the thermal properties of wood depend on the kind of tree, but even for the same species there are differences from tree to tree depending on the age, climate, moisture, etc. [19-22]. Anyway, a thermal anisotropy factor of 2 has been reported [23]. That is the reason of the huge dispersion of the literature values shown in table 1 for paper, cork and wood.

On the other hand, XPS foam consists of closed cells, which dramatically reduce the thermal conductivity of homogeneous PS. Depending on the density, the thermal conductivity varies in a range between 0.032 and 0.040 $Wm^{-1}K^{-1}$ [25,25]. Using a lock-in thermography setup, authors measured the thermal conductivity and effusivity of several XPS samples: 0.035-0.040 $Wm^{-1}K^{-1}$ and 0.38-0.51 mm^2/s respectively [26]. From the constitutive equation ($e = K/\sqrt{D}$), the thermal effusivity ranges from 54 to 57 $Ws^{0.5}m^{-2}K^{-1}$, very close to the results obtained in this work (see Table 1). In the case of Basotect® foam, the manufacturer announces a thermal conductivity smaller than 0.035 $Wm^{-1}K^{-1}$, but we have not found any measure of its thermal diffusivity or effusivity. Nevertheless, taking into account its extremely low density (6 times the air density), it is not surprising that it exhibits an effusivity as low as 25 $Ws^{0.5}m^{-2}K^{-1}$. This figure could be considered as the lower limit of this method to obtain accurate effusivity values, since the phase contrast in the frequency scan is smaller than 2º.

The uncertainty in the thermal effusivity values given in Table 1 is the standard deviation corresponding to five frequency scans performed relocating the sample each time. This standard deviation varies from about 5% for low effusivities up to 8-10% for extremely low effusivities. This result is in good agreement with the sensitivity analysis performed in section 3, which indicates that the sensitivity to e_s is reduced by a factor of 2 as the effusivity is reduced from 500 to 50 $Ws^{0.5}m^{-2}K^{-1}$ (see Fig. 5a).

5. Conclusions

In this work, we address the challenge of measuring the thermal effusivity of thermal insulators accurately. We propose a method based on the PPE technique in the front configuration because of its outstanding signal to noise ratio. We have developed a complete theoretical model of the PPE signal generation. It takes into account: (a) the thin fluid layer used to put in thermal contact the sample and the pyroelectric sensor, and (b) heat losses by convection, radiation and conduction to the surrounding gas. Moreover, to avoid damaging the sample we put it in direct contact with the pyroelectric sensor. Accordingly, a thin air layer remains between them. On the other hand, numerical simulations show that thin pyroelectric sensors are more sensitive to the sample effusivity than thicker ones. The method has been validated by measuring a homogeneous polymer of well-known thermal properties. Then, several porous materials have been measured: paper, cork, wood and foam. As expected, as the porosity grows (the density diminishes) the thermal effusivity decreases, approaching the air thermal effusivity. A thermal effusivity as low as 25 $Ws^{0.5}m^{-2}K^{-1}$ (only five times the air effusivity) was measured with an uncertainty of 10%. It can be considered as the lower limit of this method, since the phase contrast is smaller than 2º.

Acknowledgments

This work has been supported by Ministerio de Economía y Competitividad, (DPI2016-77719-R, AEI/FEDER, UE) and by Universidad del País Vasco UPV/EHU (GIU16/33).

References

[1] D. Dadarlat, M. Chirtoc, C. Nematu, R.M. Candea and D. Bicanic, Inverse photopyroelectric detection method, Phys. Status Solidi A, **121**, K231-235 (1990).
[2] S. Longuemart, A. Garcia-Quiroz, D. Dadarlat, A. Hadj Sahraoui, C. Kolinsky and J.M. Buisine, E. Correa da Silva, A.M. Mansanares, X. Filip and C. Nematu, An application of the front photopyroelectric technique for measuring the thermal effusivity of some foods, Instrum. Sci. & Technol. **30**, 157-165 (2002).
[3] A. Hadj Sahraoui, S. Longuemart, D. Dadarlat, S. Delenclos, C. Kolinsky and J.M. Buisine, The application of the photopyroelectric method for measuring the thermal parameters of pyroelectric materials, Rev. Sci. Instrum. **73**, 2766-2772 (2002).
[4] D. Dadarlat and C. Neamtu, Detection of molecular associations in liquids by photopyroelectric measurements of thermal effusivity, Meas. Sci. Technol. **17**, 3250-3254 (2006).
[5] D. Dadarlat, C. Neamtu, M. Streza, R. Turcu, I. Craciunescu, D. Bica and L. Vekas, High accuracy photopyroelectric investigation of dynamic thermal parameters of FeO and CoFeO magnetic nanofluids, J. Nanopart. Res. **10**, 1329-1336 (2008).
[6] U Zammit, F Mercuri, S Paoloni, M Marinelli and R Pizzoferrato, Simultaneous absolute measurements of the thermal diffusivity and the thermal effusivity in solids and liquids using photopyroelectric calorimetry, J. Appl. Phys. **117**, 105104, (2015)
[7] A. Salazar, A. Oleaga, V. Shvalya and E. Apiñaniz, Improved thermal effusivity measurements of solids using the photopyroelectric technique in the front configuration, Int. J. Therm. Sci. **100**, 60-65 (2016).
[8] D.P. Almond and P.M. Patel, Photothermal Science and Techniques, Chapman & Hall, London (1996).
[9] M. Depriester, P. Hus, S. Delenclos, A. Hadj Sahraoui, New methodology for thermal parameter measurements in solids using photothermal radiometry, Rev. Sci. Instrum. **76**, 074902 (2005).
[10] C. Vales-Pinzon, J. Ordonez-Miranda, J.J. Alvarado-Gil, Photothermal characterization of the thermal properties of materials using four characteristic modulation frequencies in two-layer systems, J. Appl. Phys. **112**, 064909 (2012).
[11] M. Chirtoc and G. Mihailescu, Theory of the photopyroelectric method for investigation of optical and thermal materials properties, Phys. Rev. B **40**, 9606-9617 (1989).
[12] J. Shen, A. Mandelis and H. Tsai, Signal generation mechanisms, intracavity-gas thermal-diffusivity temperature dependence, and absolute infrared emissivity measurements in a thermal-wave resonant cavity, Rev. Sci. Instrum. **69**, 197-203 (1998).
[13] J. Ordonez-Miranda and J.J. Alvarado-Gil, Infrared emissivity using a thermal-wave resonant cavity: Comparison between the length- and frequency-scan approaches, Int. J. Therm. Sci. **74**, 208-213 (2013).
[14] M. N. Özisik and H.R.B. Orlande, Inverse Heat Transfer, Taylor & Francis, New York (2000), p. 53.
[15] K. Horne, A. Fleming, B. Timmins and H. Ban, Monte Carlo uncertainty analysis for photothermal radiometry measurements using curve fit process, Metrologia **52**, 783-792 (2015).
[16] K. Martínez, E. Marín, C. Glorieux, A. Lara-Bernal, A. Calderón, G. Peña-Rodríguez and R. Ivanov, Thermal diffusivity measurements in solids by photothermal infrared radiometry: Influence of convection-radiation heat losses, Int. J. Therm. Sci. **98**, 202-207 (2015).
[17] S. A. Lavrykov and B.V. Ramarao, Thermal properties of paper sheets, Drying Technol. **30**, 297-311 (2012).

[18] S. P. Silva, M. A. Sabino, E. M. Fernandes, V. M. Correlo, L. F. Boesel and R. L. Reis, Cork: properties, capabilities and applications, International Materials Reviews **50**, 345-365 (2005).
[19] Y.A. Çengel, Heat Transfer: A practical Approach, McGraw-Hill, Boston, (2003).
[20] N.J. Kotlarewski, B. Ozarska and B.K. Gusamo, Thermal conductivity of Papua New Guinea balsa wood measured using the needle probe procedure, Bioresources **9**, 5784-5793 (2014).
[21] R. Hrčka, Variation of thermal properties of beech wood in the radial direction with moisture content and density, in Wood Structure and Properties 10, Ed. J. Kúdela and R. Lagana, Arbora Publishers, Zvolen, Slovakia, 2010. p. 111-116.
[22] A. Jankowska and P. Kozakiewicz, Comparison of thermal properties of selected wood species from Africa, Annals of Warsaw University of Life Sciences, Forestry and Wood Technology **82**, 335-338 (2013).
[23] P. Niemz, W. Sonderegger and S. Hering, Thermal conductivity of Norway spruce and European beech in the anatomical directions, Annals of Warsaw University of Life Sciences, Forestry and Wood Technology **72**, 66-72 (2010).
[24] F. Domínguez-Muñoz, B. Anderson, J.M. Cejudo-López and A. Carrillo-Andrés, Uncertainty in the thermal conductivity of insulation materials, Energy and Buildings **42**, 2159-2168 (2010).
[25] R. Coquard, E. Coment, G. Flasquin and D. Baillis, Analysis of the hot-disk technique applied to low-density insulating materials, Int. J. Therm. Sci. **65**, 242-253 (2013).
[26] A. Cifuentes, A. Mendioroz and A. Salazar, Simultaneous measurements of the thermal diffusivity and conductivity of thermal insulators using lock-in infrared thermography, Int. J. Therm. Sci. **121**, 305-312 (2017).
[27] See Goodfellow catalogue at http://www.goodfellow.com

Figure Captions

Fig. 1. Geometry of the photopyroelectric cell in the front configuration. (a) Three-layer stack and (b) bare pyroelectric sensor.

Fig. 2. Numerical simulations of the frequency dependence of the phase and amplitude of the normalized PPE signal, Ψ_n and $|S_n|$, using a $LiTaO_3$ pyroelectric sensor and a fixed coupling fluid "thermal thickness", $L_f / \sqrt{D_f}$ = 0.01 $s^{0.5}$. (a) and (b) intermediate thermal effusor (e_s = 1000 $Ws^{0.5}m^{-2}K^{-1}$). (c) and (d) low thermal effusor (e_s = 100 $Ws^{0.5}m^{-2}K^{-1}$). Two sensor thicknesses are studied. The black lines are the simulations in the absence of heat losses (e_g = 0 and h = 0) and the red lines are the simulations including heat losses (e_g = 5.5 $Ws^{0.5}m^{-2}K^{-1}$ and h = 10 $Wm^{-2}K^{-1}$).

Fig. 3. (a) Numerical simulations of the effect of the thermal thickness of the coupling fluid on the frequency dependence of the phase of the normalized PPE signal, Ψ_n. Calculations have been performed with e_s = 100 $Ws^{0.5}m^{-2}K^{-1}$, e_g = 5.5 $Ws^{0.5}m^{-2}K^{-1}$ and h = 10 $Wm^{-2}K^{-1}$. (b) Numerical simulations of the effect of heat losses by convection and radiation on the frequency dependence of the phase of the normalized PPE signal, Ψ_n. Calculations have been performed with e_s = 100 $Ws^{0.5}m^{-2}K^{-1}$, L_p = 75 μm, e_g = 5.5 $Ws^{0.5}m^{-2}K^{-1}$ and $L_f / \sqrt{D_f}$ = 0.01 $s^{0.5}$. (c) Numerical simulations of the effect of the sample effusivity on the frequency dependence of the phase of the normalized PPE signal, Ψ_n. Calculations have been performed with L_p = 75 μm, e_g = 5.5 $Ws^{0.5}m^{-2}K^{-1}$, h = 10 $Wm^{-2}K^{-1}$ and $L_f / \sqrt{D_f}$ = 0.01 $s^{0.5}$.

Fig. 4. Sensitivity of Ψ_n to the fitting parameters for a pyroelectric sensor 75 μm thick. Simulations have been performed for a low thermal effusor e_s = 100 $Ws^{0.5}m^{-2}K^{-1}$, with e_g = 5.5 $Ws^{0.5}m^{-2}K^{-1}$, h = 10 $Wm^{-2}K^{-1}$ and $L_f / \sqrt{D_f}$ = 0.01 $s^{0.5}$.

Fig. 5. (a) Frequency dependence of the sensitivity of Ψ_n to the e_s for several effusivity values. Calculations have been performed with L_p = 75 μm, e_g = 5.5 $Ws^{0.5}m^{-2}K^{-1}$, h = 10 $Wm^{-2}K^{-1}$ and $L_f / \sqrt{D_f}$ = 0.01 $s^{0.5}$. (b) Frequency dependence of the sensitivity of Ψ_n to e_s for several $L_f / \sqrt{D_f}$ values. Calculations have been performed with e_s = 100 $Ws^{0.5}m^{-2}K^{-1}$, L_p = 75 μm, e_g = 5.5 $Ws^{0.5}m^{-2}K^{-1}$ and h = 10 $Wm^{-2}K^{-1}$.

Fig. 6. Experimental frequency scans of the phase of the normalized PPE signal for a 4 mm thick polyether-ether-ketone (PEEK) plate. Two pyroelectric sensors of different thickness have been used. Dots are the experimental data and the continuous lines are the fittings to Eq. (6).

Fig. 7. Experimental frequency scans of the phase of the normalized PPE signal for: (a) Isotropic thermal insulators and (b) anisotropic ones. For them, measurements have been performed in two directions: perpendicular and parallel to the growth rings. Dots are the experimental data and the continuous lines are the fittings to Eq. (6).

Table 1. Room temperature thermal effusivity (e_s) of the materials studied in this work.

Material	e_s ($Ws^{0.5}m^{-2}K^{-1}$)	e_s Literature[a] ($Ws^{0.5}m^{-2}K^{-1}$)
PEEK	675±45 (thick sensor)	655
PEEK	670±35 (thin sensor)	655
Watercolour paper	305±18	-
Cork	180±13	85-105
XPS yellow	54±4	54-57
XPS green	52±4	54-57
Basotect©	25±3	-
Beech wood ⊥	360±25	300-460
Beech wood ‖	515±30	300-460
Balsa wood ⊥	154±10	110-200
Balsa wood ‖	200±15	110-200

[a]References [19,26,27]

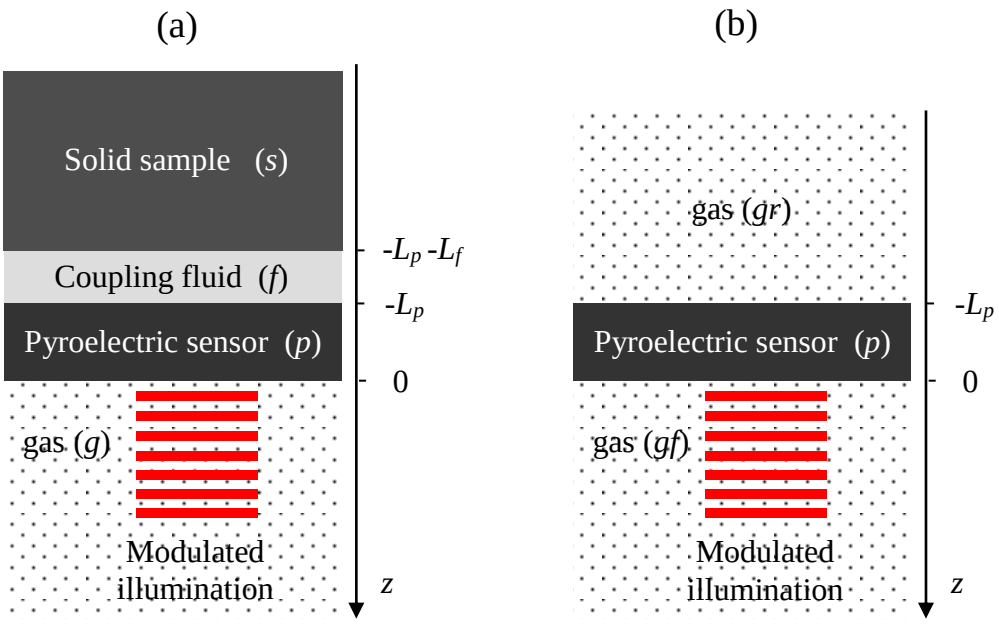
(a)
(b)
Solid sample (s)
Coupling fluid (f)
Pyroelectric sensor (p)
gas (g)
Modulated illumination
-Lp -Lf
-Lp
0
z
gas (gr)
Pyroelectric sensor (p)
gas (gf)
Modulated illumination
-Lp
0
z

Fig. 1

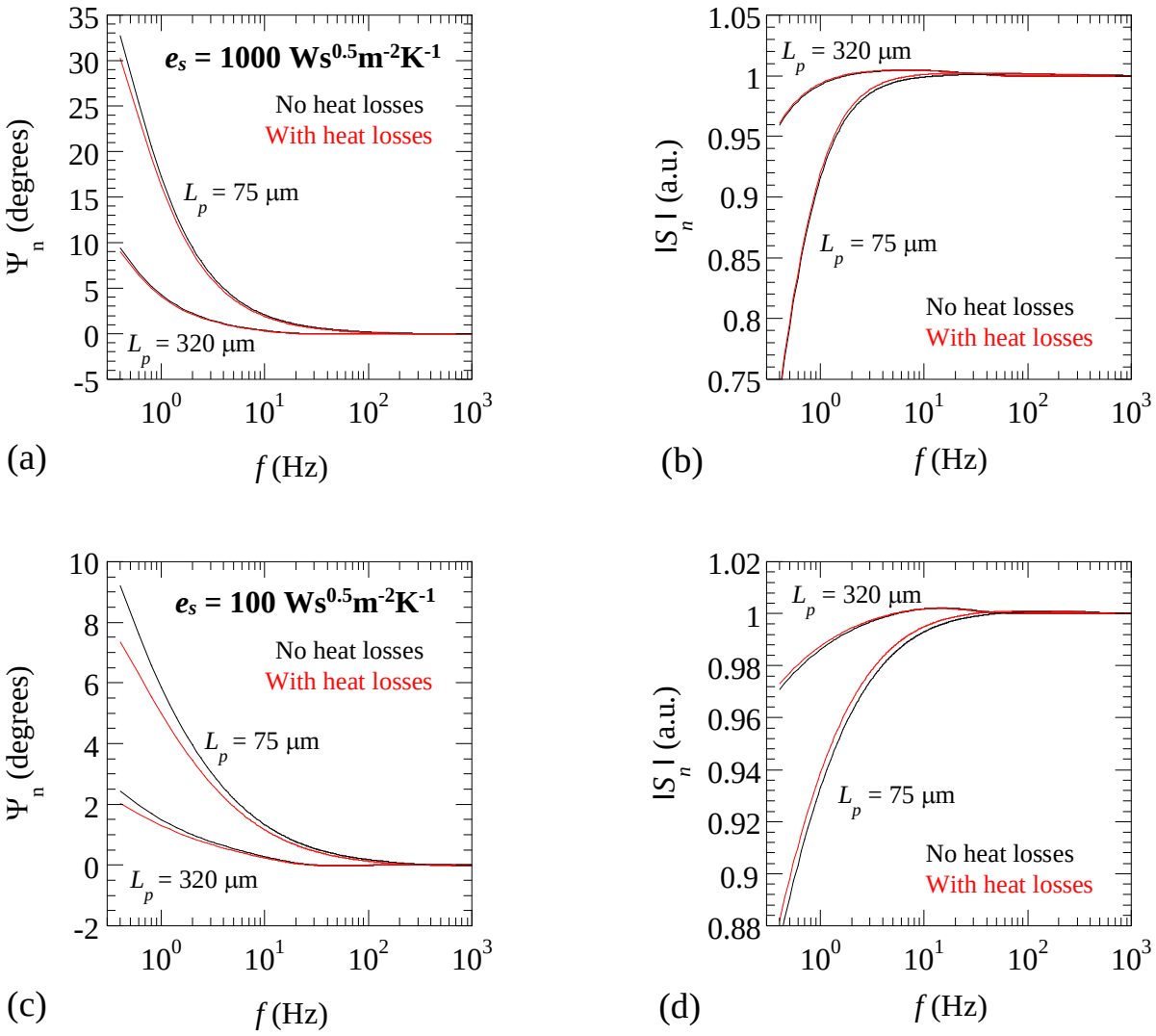
(a)
e_s = 1000 Ws$^{0.5}$m^{-2}K^{-1}
No heat losses
With heat losses
L_p = 75 µm
L_p = 320 µm
Ψ$_n$ (degrees)
f (Hz)
(b)
L_p = 320 µm
L_p = 75 µm
No heat losses
With heat losses
|S|$_n$ (a.u.)
f (Hz)
(c)
e_s = 100 Ws$^{0.5}$m^{-2}K^{-1}
No heat losses
With heat losses
L_p = 75 µm
L_p = 320 µm
Ψ$_n$ (degrees)
f (Hz)
(d)
L_p = 320 µm
L_p = 75 µm
No heat losses
With heat losses
|S|$_n$ (a.u.)
f (Hz)

Fig. 2

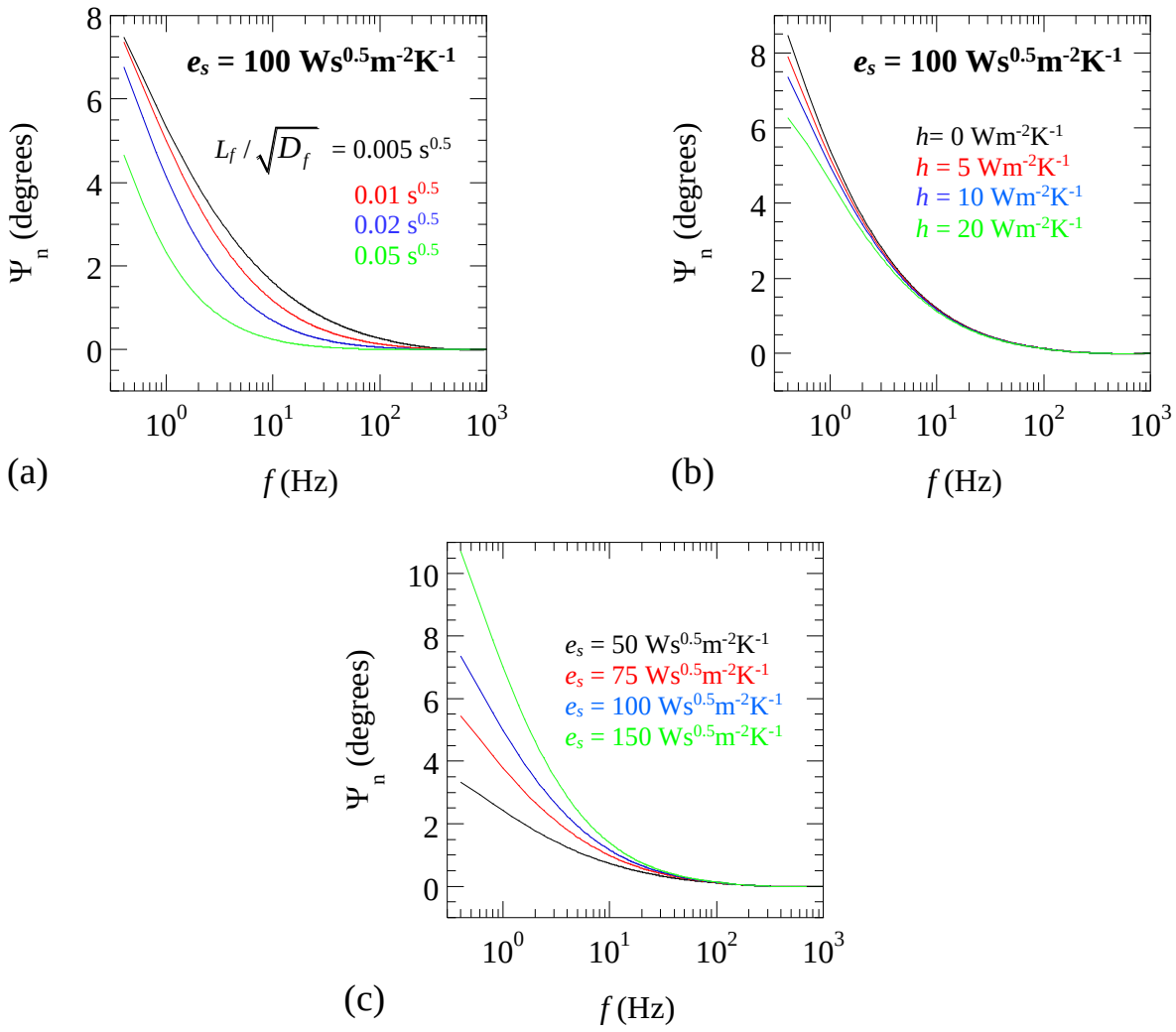
e_s = 100 Ws$^{0.5}$m^{-2}K^{-1}
$L_f / \sqrt{D_f}$ = 0.005 s$^{0.5}$
0.01 s$^{0.5}$
0.02 s$^{0.5}$
0.05 s$^{0.5}$
Ψ_n (degrees)
f (Hz)
(a)
e_s = 100 Ws$^{0.5}$m^{-2}K^{-1}
h= 0 Wm^{-2}K^{-1}
h = 5 Wm^{-2}K^{-1}
h = 10 Wm^{-2}K^{-1}
h = 20 Wm^{-2}K^{-1}
Ψ_n (degrees)
f (Hz)
(b)
e_s = 50 Ws$^{0.5}$m^{-2}K^{-1}
e_s = 75 Ws$^{0.5}$m^{-2}K^{-1}
e_s = 100 Ws$^{0.5}$m^{-2}K^{-1}
e_s = 150 Ws$^{0.5}$m^{-2}K^{-1}
Ψ_n (degrees)
f (Hz)
(c)

Fig. 3

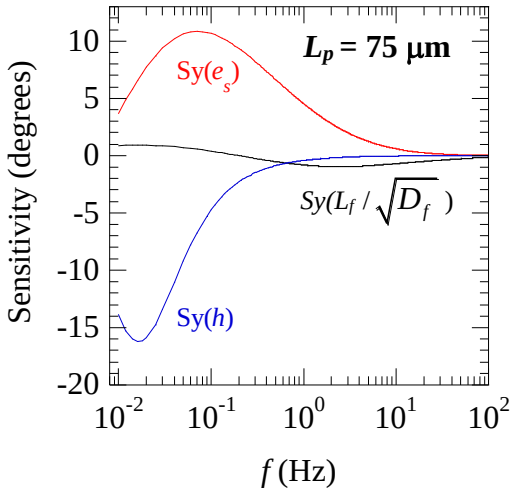
L_p = 75 µm
Sy(e_s)
Sy(L_f / $\sqrt{D_f}$)
Sy(h)
Sensitivity (degrees)
10
5
0
-5
-10
-15
-20
10^{-2}
10^{-1}
10^{0}
10^{1}
10^{2}
f (Hz)

Fig. 4

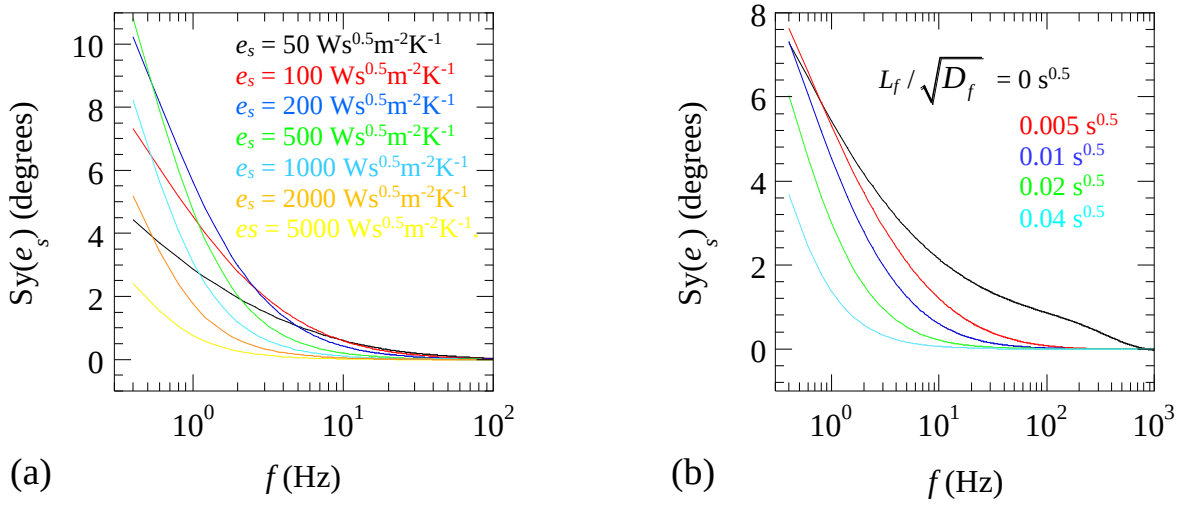
e_s = 50 Ws$^{0.5}$m^{-2}K^{-1}
e_s = 100 Ws$^{0.5}$m^{-2}K^{-1}
e_s = 200 Ws$^{0.5}$m^{-2}K^{-1}
e_s = 500 Ws$^{0.5}$m^{-2}K^{-1}
e_s = 1000 Ws$^{0.5}$m^{-2}K^{-1}
e_s = 2000 Ws$^{0.5}$m^{-2}K^{-1}
es = 5000 Ws$^{0.5}$m^{-2}K^{-1}
Sy(e_s) (degrees)
f (Hz)
(a)
L_f / $\sqrt{D_f}$ = 0 s$^{0.5}$
0.005 s$^{0.5}$
0.01 s$^{0.5}$
0.02 s$^{0.5}$
0.04 s$^{0.5}$
Sy(e_s) (degrees)
f (Hz)
(b)

Fig. 5

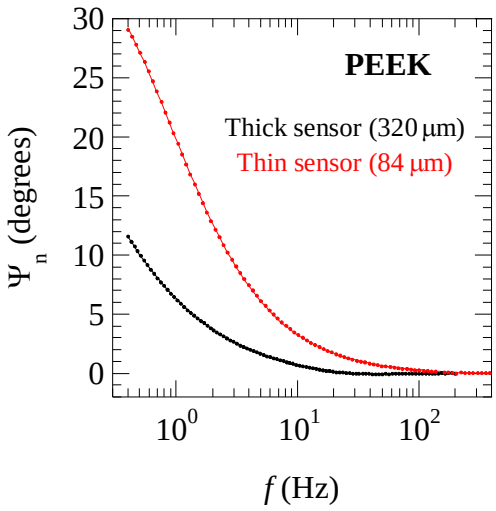
PEEK
Thick sensor (320 μm)
Thin sensor (84 μm)
Ψ n (degrees)
f (Hz)

Fig. 6

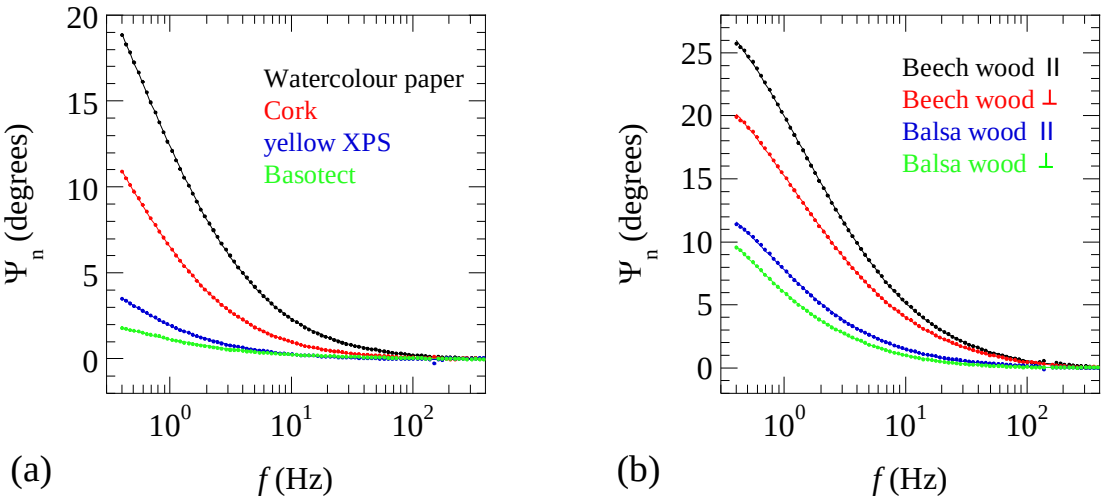
Watercolour paper
Cork
yellow XPS
Basotect
Ψ n (degrees)
f (Hz)
(a)
Beech wood ∥
Beech wood ⊥
Balsa wood ∥
Balsa wood ⊥
Ψ n (degrees)
f (Hz)
(b)

Fig. 7